RESEARCH ARTICLE | MARCH 23 2026

Tunable integrated ring resonators by femtosecond laser micromachining

Giulio Gualandi ; Fabio Saretto; Daniele Pedroli ; Giacomo Corrielli ; Marco Liscidini ; Roberto Osellame ; Andrea Crespi

APL Photonics 11, 036110 (2026)
https://doi.org/10.1063/5.0311625

Tunable integrated ring resonators by femtosecond laser micromachining

Cite as: APL Photon. 11, 036110 (2026); doi: 10.1063/5.0311625
Submitted: 11 November 2025 • Accepted: 9 March 2026 •
Published Online: 23 March 2026

Giulio Gualandi,[1,2] Fabio Saretto,[1] Daniele Pedroli,[3] Giacomo Corrielli,[2,4] Marco Liscidini,[2,3] Roberto Osellame,[2,4] and Andrea Crespi[1,2,a)]

AFFILIATIONS

[1] Dipartimento di Fisica-Politecnico di Milano, Piazza Leonardo da Vinci 32, 20133 Milano, Italy
[2] Istituto di Fotonica e Nanotecnologie-Consiglio Nazionale delle Ricerche (IFN-CNR), Piazza Leonardo da Vinci 32, 20133 Milano, Italy
[3] Dipartimento di Fisica "A. Volta"-Università di Pavia, Via Bassi 6, 27100 Pavia, Italy
[4] Ephos, Viale Decumano 34, 20157 Milano, Italy

[a)] **Author to whom correspondence should be addressed:** andrea.crespi@polimi.it

ABSTRACT

Femtosecond Laser Micromachining (FLM) is a powerful technology for the fabrication of photonic devices. In this context, the integration of resonant elements within the platform represents a key advancement, enhancing both its versatility and its compatibility with a wide range of optical and fluidic components specifically enabled by this technique. Here, we report the realization of a tunable racetrack resonator fabricated by FLM and operating at telecom wavelengths. Leveraging low-loss waveguides, we obtained a Q factor of the resonator as high as 8×10^5 at critical coupling. Moreover, by integrating two thermo-optic phase shifters, we achieved both resonance tuning and dynamic control of the Q factor. This capability makes the device highly versatile for applications requiring dynamic spectral control, such as tunable filters, gyroscopes, and sensors.

I. INTRODUCTION

Optical resonators are fundamental building blocks in photonic integrated circuits (PIC), as their intrinsic properties make them suitable for a broad spectrum of applications, including filters,[1,2] modulators,[3,4] sensors,[5] gyroscopes,[6,7] and nonlinear optics enhancement.[8,9] When dealing with integrated dielectric systems, ring resonators are arguably among the most versatile and successful implementations. A ring resonator is essentially a waveguide bent into a closed loop that confines light to circulate within it. In this configuration, the resonant frequencies are determined by the interplay between the dispersion relation of the waveguide modes and the loop length. Coupling light into and out of the resonator is typically achieved through evanescent coupling, by placing one or more access waveguides in close proximity to the ring.[10]

The realization of ring resonators in a given photonic platform strongly depends on refractive index contrast and the adopted fabrication technology. For example, in silicon-on-insulator (SOI) photonic platforms, the large refractive index contrast allows one to fabricate very compact structures with radii of only a few micrometers at telecom wavelengths while still maintaining long photon dwelling times.[11,12] However, if the refractive index contrast decreases, bending losses increasingly limit the achievable light confinement, making it necessary to adopt larger radii. This is the case, for instance, when the material of choice is silicon nitride. In fact, with this material, low-loss microrings typically have radii in the tens to hundreds of micrometers.[13,14]

Femtosecond Laser Micromachining (FLM) has emerged over the last two decades as a versatile and powerful platform for the fabrication of photonic integrated circuits (PICs), offering intrinsic three-dimensional capabilities and rapid prototyping in glass substrates.[16–18] In this material platform, however, the realization of ring resonators presents particular challenges, as FLM waveguides are formed by local refractive index modification induced by laser irradiation, for which the resulting index contrast is extremely low, typically in the range of 10^{-3}–10^{-4}. This imposes the use of bending radii on the order of millimeters to centimeters to mitigate radiation losses. Moreover, when inscribing a closed loop, undesired

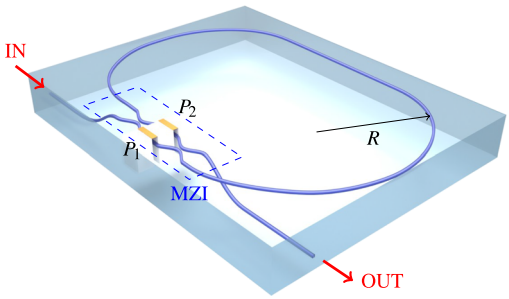

FIG. 1. Layout of the resonator. The waveguide, starting from the input port (IN), first forms a ring with a racetrack geometry, then couples back to itself through a MZI and is finally brought to the output (OUT) port, passing underneath the ring structure. The MZI is equipped with two TOPS, one per each arm, consisting in metal resistors deposited and patterned on the substrate surface. Different electrical powers P_1 and P_2 can be dissipated on the resistors, enabling independent control on the MZI phases. To enhance thermal efficiency, U-trenches were ablated around the waveguide segments.[15] The total footprint of the device is 5×6 cm^2.

inhomogeneities may arise at the overlap region where the beginning and end of the irradiated track meet, further complicating the fabrication of high-quality resonators. Such technological limitations have so far hindered the demonstration of FLM-based ring resonators.

In this work, we report the realization and experimental characterization of reconfigurable integrated optical resonators fabricated by FLM providing a design approach to overcome the issues associated with inscription inhomogeneities. Our devices are realized according to the layout depicted in Fig. 1, with a single waveguide that couples to itself through a Mach–Zehnder interferometer (MZI) and then reaches the output by passing below the ring structure. Two thermo-optic phase shifters (TOPSs) are realized on the internal arms of the MZI. By controlling the thermal powers P_1 and P_2 dissipated on the TOPS it is possible to actively tune both the wavelength shift of the spectral resonances and the Q factor of the device.

II. DEVICE DESIGN AND FABRICATION

The device design exploits the three-dimensional capabilities of FLM to realize a monolithic resonator formed from a single physically open waveguide that simultaneously functions as the resonator and as the input–output channel. In this way, one avoids the additional losses that can occur at the junction when fabricating fully closed loops with FLM. Furthermore, by exploiting the three-dimensionality of the waveguide paths, we also demonstrate the fabrication of several concentric resonators within the same glass chip: the straight sections of the waveguides are inscribed at a depth of 55 μm below the glass surface, while the bent sections forming the rings are inscribed at 35 μm, enabling vertical stacking without optical crosstalk. The additional details on the device geometry are provided in the supplementary material.

We fabricated 20 concentric resonators in a single substrate of Corning Eagle XG glass of 5×6 cm^2 footprint, using curvature radii R in the range between 16.8 and 21.0 mm. The waveguides were inscribed by four overlapped laser scans, translating the substrate with respect to the laser focus using three-axis air-bearing stages (Aerotech ABL1500) with sub-micron accuracy. In detail, we used laser pulses of 480-nJ energy, 180 fs duration, and 1 MHz repetition rate from a commercial Yb:based system emitting at 1030 nm wavelength (LightConversion Pharos). Laser pulses were focused in the substrate by a 0.5 NA water-immersion objective. Two different translations speeds were employed (5 and 7 mm s^{-1}). After laser irradiation, the substrate underwent thermal annealing post-processing to improve the optical properties of the waveguides.[19,20] These fabrication parameters ensure single-mode guiding at 1550 nm wavelength with a mode diameter ($1/e^2$) of about 7.5 μm, and propagation loss <0.2 dB/cm. TOPS were fabricated as in Ref. 15: hollow trenches were defined around the MZI arms, using water-assisted laser ablation, to provide thermal insulation; a 100-nm Cr/Au layer was deposited onto the substrate, and the resistor geometry was patterned by femtosecond laser ablation (see the supplementary material for further details). Such microstructured layout enables high-efficiency actuation (with typical electrical power values on the order of tens of mW), low crosstalk between the two TOPS, and reduces the heated area on the substrate, thus limiting thermal drifts of the optical properties of the resonator. The device was finally glued to a custom aluminum basis to improve thermal stability.

III. DEVICE OPERATION THEORY

We now describe in more detail the operating principles of the device sketched in Fig. 1. At its core lies an MZI that functions as a reconfigurable coupler, operating on the two distinct input waveguide modes a transformation described by the matrix $U = [u_{ij}]$. In particular, the coupling properties are governed by the phase shifts ϕ_1 and ϕ_2 accumulated in the two arms, which can be controlled by varying the corresponding TOPSs. In the ideal case of perfectly balanced (i.e., 50:50) directional couplers and negligible losses, the cross-coupling coefficient of the MZI is equal to

$$u_{11} = u_{22} = te^{j\phi_{cm}} = \cos\left(\frac{\Delta\phi}{2}\right)e^{j\phi_{cm}}, \tag{1}$$

where $\phi_{cm} = \frac{1}{2}(\phi_1 + \phi_2 + \pi)$ is the total phase accumulated in the MZI and $t = \cos\left(\frac{\Delta\phi}{2}\right)$ is a real coefficient, which depends on the phase difference between the two MZI arms $\Delta\phi = \phi_1 - \phi_2$ (see the supplementary material). By taking into account the thermal crosstalk between the two TOPSs, the dependence of ϕ_{cm} and $\Delta\phi$ on the dissipated electrical power P_1 and P_2 can be expressed as[21]

$$\Delta\phi = \frac{2\pi}{\lambda_0}[a_1P_1 + a_2P_2 + \Delta L], \tag{2}$$

$$\phi_{cm} = \frac{2\pi}{\lambda_0}[b_1P_1 + b_2P_2 + L] + \frac{\pi}{2}, \tag{3}$$

where λ_0 is the light wavelength in vacuum, a_i and b_i are coefficients depending on the device geometry and material properties, L is an effective optical path length of the MZI (thus taking into account also the effect of the refractive index), and ΔL is the optical-length imbalance of the MZI arms introduced by fabrication tolerances.

The power transmission of the device is given by the following expression (see supplementary material and Ref. 22):

$$\mathscr{T} = \frac{\alpha^2 + t^2 - 2\alpha t\,\cos(\theta_R + \phi_{\rm cm})}{1 + \alpha^2 t^2 - 2\alpha t\,\cos(\theta_R + \phi_{\rm cm})}, \tag{4}$$

where α is the amplitude transmission per round trip and θ_R is the phase accumulated per round trip excluding the MZI section. Finally, it is convenient to associate the round-trip phase appearing in (4) with an effective total optical path length $L_{\rm tot}$ defined as

$$\theta_R + \phi_{cm} = \frac{2\pi}{\lambda_0} L_{\rm tot}. \tag{5}$$

Since in our structure the round trip in the resonators includes the MZI, $L_{\rm tot}$ depends also on P_1 and P_2 [see (3)] and is not simply linked to the physical length of the device. However, as in the case of conventional ring resonators, a resonant wavelength $\lambda_{0,m}$ satisfies the relation $m\lambda_{0,m} = L_{\rm tot}$, with m indicating the resonance order. Similarly, the device transmission shows dips that are, for a sufficiently small spectral range, periodic in wavelength with a free spectral range FSR $= \frac{\bar{\lambda}_0^2}{L_{\rm tot}}$, where $\bar{\lambda}_0$ is the mean wavelength in vacuum in the interval of interest (here, it can safely be taken as $\bar{\lambda}_0 = 1550$ nm).

Another figure of merit characterizing the performance of optical resonators is the Q factor, defined as the ratio between the resonance frequency and the full width at half maximum (FWHM) of the corresponding spectral dip. In our case, one can show that[23]

$$Q = \frac{\lambda_0}{\rm FWHM} = \frac{\pi L_{\rm tot}}{\lambda_0}\left(\arccos\frac{2\alpha|t|}{1+\alpha^2|t|^2}\right)^{-1}. \tag{6}$$

This parameter is intrinsically related both to the round-trip losses and to the optical length of the loop.

It is worth noting that, while the common phase $\phi_{\rm cm}$ determines a shift in the resonances, the phase difference $\Delta\phi$ governs $|t|$ and, thus, modulates the depth of the transmission dips and the Q factor. Critical coupling is achieved when the MZI transmission equals the ring transmission, namely $|t| = \alpha$; in this condition, complete destructive interference ($\mathscr{T} = 0$) is achieved at resonance.

IV. EXPERIMENTAL RESULTS

All the fabricated devices were characterized by measuring the transmission spectrum in different coupling conditions, namely with different values of $|t|$. In detail, horizontally polarized coherent light from a tunable C-band laser source (Santec TLS-570) was coupled to the device input using an aspherical lens (0.18 NA). The transmitted light is collected from the output port using another aspherical lens (0.4 NA) and directed to an amplified photodiode (Thorlabs PDA10CS2). The laser wavelength was continuously swept over a 160 pm range starting from 1550.000 nm at 1 nm/s speed, while the photodiode signal was recorded by a digital oscilloscope. An example of the resulting transmission spectrum is shown in Fig. 2(a). To study different coupling conditions, corresponding to different values of $|t|$, we measured the transmission for different values of the dissipated power P_1 on the first TOPS, leaving $P_2 = 0$.

From the acquired spectrum, we can experimentally retrieve both the FWHM and the FSR of the transmission dips [see also Fig. 2(b)], as averages of the widths and of the distances of the resonance dips found in the acquired wavelength range.

In addition, from each spectrum, we extracted the minimum ($V_{\rm min}$) and maximum values ($V_{\rm max}$) of the signal. Figure 2(c) plots $V_{\rm min}$ and $V_{\rm max}$ as a function of P_1 (respectively, the blue and red curves), as an example in the case of the device with $R = 19.8$ mm. The maximum and minimum of the red curve correspond to the cases of minimal $|t| \sim 1$ and maximal $|t| \sim 0$ coupling to the ring, respectively. Importantly, these values can be used to estimate experimentally the internal round-trip losses of the resonator using

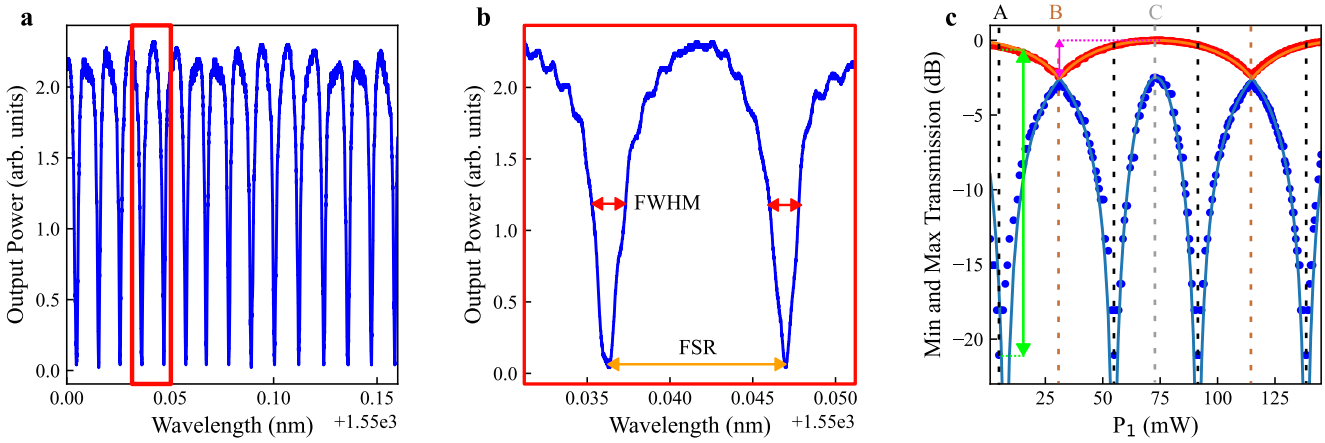

FIG. 2. Characterization of the spectral response of the resonator. (a) Output power of the resonator as a function of wavelength under critical coupling conditions. Multiple resonance dips are visible over a span of 160 pm. (b) Zoom-in of the spectral region highlighted by the red rectangle in (a), showing the shape and depth of individual resonance fringes, with the FWHM and FSR indicated by red and orange arrows, respectively. (c) Maximum (red dot) and minimum (blue dot) transmission values extracted from the spectra as P_1 is varied (thereby tuning the coupling coefficient t), plotted in logarithmic scale, with 0 dB corresponding to the overall maximum measured transmission value. The solid lines represent a theoretical fit, taking into account unbalanced directional couplers; see text. The dotted line labeled A (black), B (brown), and C (gray) correspond to $|t| = \alpha$ (critical coupling condition), strong overcoupling ($|t| \sim 0$), and strong undercoupling ($|t| \sim 1$). The purple arrow indicates the internal losses of the ring, while the green arrow marks the extinction ratio achieved experimentally at critical coupling.

$$\left.\frac{1}{\alpha^2}\right|_{\mathrm{dB}} = -10\log_{10}\left(\frac{\min\{V_{\max}\}}{\max\{V_{\max}\}}\right). \quad (7)$$

The measured losses are reported in Fig. 3(a) for all fabricated resonators. The increase in loss with the curvature radius is primarily due to the longer loop length, showing that propagation losses in the waveguides are dominant with respect to additional losses due to bending, for the tested radii. Waveguides written at a speed of 7 mm s^{-1} demonstrate significantly better performance, consistently remaining below 3 dB overall loss. In particular, the device with R = 17.4 mm yields the minimum loss of about 1.9 dB, over a loop geometrical length of 127.6 mm.

The vertical distance between the blue and the red curve in the graph of Fig. 2(c) gives the extinction ratio of the transmission dips for a given value of P_1. The maximum extinction ratio is achieved at the critical coupling points, where $|t| = \alpha$. If the directional couplers of the MZI were perfectly balanced, by varying P_1 we would be able to scan the full interval of values of $|t|$ from 0 to 1 following precisely (1); in this ideal case, the maxima of the blue curve would touch the red curve, resulting from a flat transmission spectrum at those points. The distance between the curves still observed in those points indicates that $|t| = 0$ and $|t| = 1$ cannot be achieved precisely due to imperfections in the directional couplers of the MZI.

In fact, we also report as a solid line the fit from a theoretical model, which includes the possibility of unbalanced couplers (but still equal one to the other) composing the MZI. As shown in Fig. 2(c), the experimental points are well reproduced by assuming 64:36 power splitting ratio of the individual couplers (see the supplementary material for additional details). This improved theoretical model would still predict vanishing transmission at the minima, whereas, in practice, a finite residual background is observed. This is likely due to the non-negligible spectral bandwidth of the tunable laser; other small deviations between the data and the fitted curve are attributable to the nonuniform wavelength scanning of the laser.

Figure 3(b) reports the measured FSR values for all devices, compared to a theoretical curve calculated as $FSR = \tilde{\lambda}_0^2/L_{\mathrm{tot}} = \tilde{\lambda}_0^2/(n_g\mathscr{L})$, where $\mathscr{L}$ is the nominal geometrical length of the waveguide loop (counting both the length of the race-track and the length of the MZI waveguides). In the 160-pm wide wavelength range studied here, dispersion can be safely neglected, and in the latter formula, we use $n_g = n = 1.49$ from Ref. 24.

Finally, Fig. 3(c) reports the quality factor Q_{cc} at the critical coupling condition for all the fabricated devices. The quality factor at the critical coupling is $Q_{\mathrm{cc}} = Q_i/2$, with Q_i the intrinsic quality factor, and hence it depends only on the propagation losses per unit of length α_L of the ring waveguide according to $Q_{\mathrm{cc}} = \pi n_g/(\lambda_0\alpha_L)$ (see the supplementary material for additional details). Thus, from the results shown in Fig. 3(c), one can directly estimate the propagation losses per unit of length, which are about 0.23 ± 0.02 dB/cm for 5 mm/s writing speed and of about 0.17 ± 0.02 dB/cm for 7 mm/s. Such losses are essentially independent of radii, with small fluctuation from sample to sample. This indicates negligible bending losses for radii larger than 17 mm for both fabrication speed. As a further check, inverting (6) with these Q factor values yields round-trip losses in good agreement with those previously determined. The best-performing resonator exhibits $Q_{\mathrm{cc}} \approx 8.3 \times 10^5$ corresponding to $Q_i \approx 1.6 \times 10^6$.

The propagation and bending loss demonstrated here are well-aligned with the state of the art of our technology in this kind of substrate and for telecom wavelengths.[19,20,25] Based on what has been reported in the literature for waveguides fabricated with similar parameters, it is reasonable to expect that bending losses become increasingly significant for radii smaller than 15 mm. Specific waveguide irradiation strategies (see, e.g., Ref. 25) may enable smaller bending radii, at the expense of higher propagation loss and reduced Q-factor.

As mentioned, the Q factor changes with the coupling condition defined by the MZI that in our device can be tuned actively. Figure 4 shows the Q factor as a function of the dissipated power P_1,

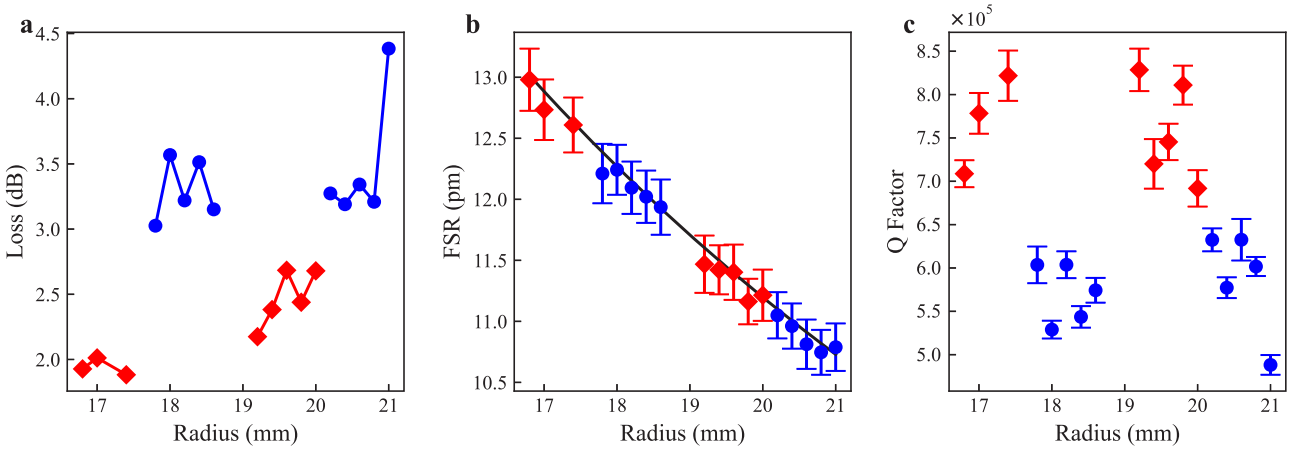

FIG. 3. Characterization of all resonators as a function of the ring radius, where blue dotted markers represent the values obtained with a writing speed of 5 mm s^{-1}, while red diamonds correspond to those fabricated at 7 mm s^{-1}. (a) Measured round-trip losses of the ring resonator. (b) Free Spectral Range (FSR), where the green line represents the theoretical prediction based on the relation FSR = $\frac{\tilde{\lambda}^2}{L_{\mathrm{tot}}}$, and the data points indicate measured values, calculated by averaging the separation between resonance dips detected over the scanned wavelength range. (c) Quality factor of each resonator, extracted from the FWHM under critical coupling conditions.

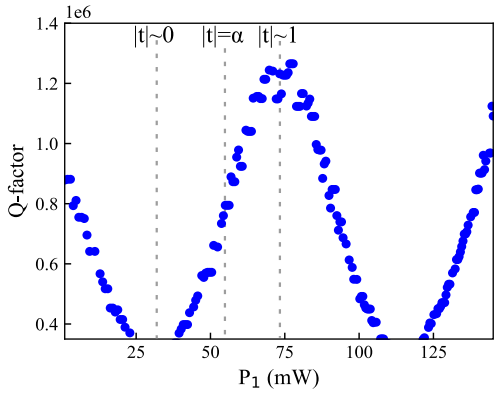

FIG. 4. Q factor as a function of dissipated power P_1, illustrating the transition between coupling regimes, from strong overcoupling ($|t| \sim 0$) to strong undercoupling ($|t| \sim 1$), passing from critical coupling ($|t| = \alpha$). The highest Q factor is observed in undercoupling regime. No data points are shown around the minima, as the transmission spectrum becomes flat in those regions, preventing the identification of a resonance dip and, consequently, the measurement of a meaningful FWHM.

calculated from the FWHM of the spectral dips, in the case of the device with $R = 19.8$ mm. The plot highlights three notable coupling conditions: critical coupling ($|t| = \alpha$), strong overcoupling ($|t| \approx 0$), and strong undercoupling ($|t| \approx 1$). The highest Q factor is observed in the undercoupling regime.

Finally, we show that by simultaneously actuating both TOPSs on the two MZI arms, we can tune the position of the resonances. We scan the power P_2 on the second TOPS, while adjusting at the same time P_1 according to

$$P_1 = P_{1,cc} - \frac{a_2}{a_1} P_2, \tag{8}$$

where $P_{1,cc}$ is the dissipated power that produces the critical coupling condition when $P_2 = 0$ (namely, $\frac{2\pi}{\lambda_0}(a_1 P_{1,cc} + \Delta L) = \Delta\phi_{cc}$ that gives $|t| = \alpha$). In this way, we ensure that the phase shift difference $\Delta\phi$ in the MZI remains constant, thereby maintaining the critical coupling condition. At the same time, the common phase ϕ_{cm} is varied, effectively modifying the total phase accumulated in the ring. The values of the coefficients a_1 and a_2 were estimated by a preliminary characterization of the response of each TOPS separately (see the supplementary material for further detail). For each value of P_2, we recorded the transmission spectrum, which was then convoluted with a reference one acquired with $P_2 = 0$, to accurately extract the wavelength shift of the dips. The results are shown in Fig. 5, together with a linear fit. We are able to change the position of the peak by more than 15 pm, namely more than one FSR, in this case in the order of 11 pm. This demonstrates complete tunability of the device.

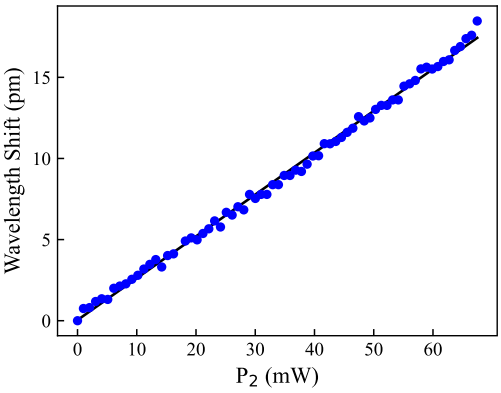

FIG. 5. Diagram showing the resonance shift as a function of the dissipated power P_2. The data show a clear linear trend, highlighted by the black linear fit.

V. CONCLUSIONS

We have demonstrated the tunable integrated ring resonators fabricated using FLM, reaching a Q factor above 8×10^5 at critical coupling. By actuating judiciously the two TOPS on the MZI that couples the ring resonator to the waveguide, we demonstrate precise tuning of the resonance position over more than one FSR, and the capability to change the Q factor actively. This capability makes our device versatile and of potential interest for applications requiring dynamic control of the spectral response, including tunable optical filters, gyroscopes, and other sensing systems. Due to the inherently low thermo-optic coefficient of silica glass and to the high control on the heat diffusion in our microstructured TOPS, this platform may offer improved thermal stability compared to silicon-based technologies. Notably, this demonstration paves the way to innovative devices, integrating ring resonators with other three-dimensional optical or fluidic devices uniquely enabled by the capabilities of the FLM technology.

SUPPLEMENTARY MATERIAL

The supplementary material reports additional information about: the device design and fabrication, the physical modelling of the device opertion, the curve fitting in Fig. 2(c), the experimental procedure to estimate coefficients a_1 and a_2 in Eq. (8), the relation between optical loss and Q factor.

ACKNOWLEDGMENTS

G.C. and R.O. acknowledge funding from the European Innovation Council through the EIC Transition project FUTURE (Grant No. 101136471).

AUTHOR DECLARATIONS

Conflict of Interest

M.L. and R.O. have a patent application related to the device described in this article. All other authors have no conflicts to disclose.

Author Contributions

Giulio Gualandi: Formal analysis (equal); Investigation (lead); Writing – original draft (equal); Writing – review & editing (equal). **Fabio Saretto**: Formal analysis (equal); Investigation (lead);

Writing – review & editing (equal). **Daniele Pedroli**: Formal analysis (equal); Writing – review & editing (equal). **Giacomo Corrielli**: Conceptualization (supporting); Funding acquisition (equal); Investigation (supporting); Writing – review & editing (equal). **Marco Liscidini**: Conceptualization (lead); Formal analysis (equal); Supervision (equal); Writing – review & editing (equal). **Roberto Osellame**: Conceptualization (lead); Funding acquisition (equal); Supervision (equal); Writing – review & editing (equal). **Andrea Crespi**: Conceptualization (supporting); Formal analysis (equal); Investigation (supporting); Writing – original draft (equal); Writing – review & editing (equal).

DATA AVAILABILITY

The data that support the findings of this study are available within the article and its supplementary material. Numerical data at the basis of the graphs reported in the Main Text are openly available in Zenodo at https://doi.org/10.5281/zenodo.17657882.

REFERENCES

[1] D. H. Geuzebroek and A. Driessen, "Ring-resonator-based wavelength filters," in *Wavelength Filters in Fibre Optics*, *Springer Series in Optical Sciences*, edited by L. Cheng (Springer, 2006), Vol. 123, pp. 341–379.

[2] J. Xu, Y. Zhang, X. Guo, Q. Huang, X. Zhang, and Y. Su, "Ultra-narrow passband-tunable filter based on a high-Q silicon racetrack resonator," Opt. Lett. **46**, 5575–5578 (2021).

[3] Y. Yuan, Y. Peng, W. V. Sorin, S. Cheung, Z. Huang, D. Liang, M. Fiorentino, and R. G. Beausoleil, "A 5 × 200 Gbps microring modulator silicon chip empowered by two-segment z-shape junctions," Nat. Commun. **15**, 918 (2024).

[4] J. Hong, F. Qiu, X. Cheng, A. M. Spring, and S. Yokoyama, "A high-speed electro-optic triple-microring resonator modulator," Sci. Rep. **7**, 4682 (2017).

[5] A. Sarkaleh, B. Lahijani, H. Saberkari, and A. Esmaeeli, "Optical ring resonators: A platform for biological sensing applications," J. Med. Signals Sens. **7**, 185–191 (2017).

[6] Y. H. Lai, M. G. Suh, Y. K. Lu, B. Shen, Q. F. Yang, H. Wang *et al.*, "Earth rotation measured by a chip-scale ring laser gyroscope," Nat. Photonics **14**, 345–349 (2020).

[7] P. P. Khial, A. D. White, and A. Hajimiri, "Nanophotonic optical gyroscope with reciprocal sensitivity enhancement," Nat. Photonics **12**, 671–675 (2018).

[8] P. Tritschler, C. Schweikert, R. H. Klenk, S. Abdani, O. Sözen, W. Vogel, G. Rademacher, T. Ohms, A. Zimmermann, and P. Degenfeld-Schonburg, "Nonlinear optical bistability in microring resonators for enhanced phase sensing," Phys. Rev. Lett. **134**, 123802 (2025).

[9] P. Tritschler, T. Ohms, C. Schweikert, O. Sözen, R. H. Klenk, S. Abdani, W. Vogel, G. Rademacher, A. Zimmermann, and P. Degenfeld-Schonburg, "Chip-integrated single-mode coherent-squeezed light source using four-wave mixing in microresonators," arXiv:2502.16278 (2025).

[10] D. G. Rabus and C. Sada, "Building blocks of ring resonator devices," in *Integrated Ring Resonators: A Compendium*, *Springer Series in Optical Sciences*, edited by D. G. Rabus and C. Sada (Springer International Publishing, Cham, 2020), Vol. 127, pp. 179–198.

[11] W. Bogaerts, P. De Heyn, T. Van Vaerenbergh, K. De Vos, S. Kumar Selvaraja, T. Claes, P. Dumon, P. Bienstman, D. Van Thourhout, and R. Baets, "Silicon microring resonators," Laser Photonics Rev. **6**, 47–73 (2012).

[12] R. Guo, Q. He, Z. Zhang, Y. Xu, S. Zhang, Q. Lang, S. Xiao, P. Han, J. Wang, T. Ding, T. Liu, H. K. Tsang, K. Goda, and Z. Cheng, "High-Q silicon microring resonator with ultrathin sub-wavelength thicknesses for sensitive gas sensing," Appl. Phys. Rev. **11**, 021417 (2024).

[13] X. Ji, F. A. S. Barbosa, S. P. Roberts, A. Dutt, J. Cardenas, Y. Okawachi, A. Bryant, A. L. Gaeta, and M. Lipson, "Ultra-low-loss on-chip resonators with sub-milliwatt parametric oscillation threshold," Optica **4**, 619–624 (2017).

[14] S. Cui, K. Cao, Z. Pan, X. Gao, Y. Yu, and X. Zhang, "Compact microring resonator based on ultralow-loss multimode silicon nitride waveguide," Adv. Photonics Nexus **2**, 046007 (2023).

[15] F. Ceccarelli, S. Atzeni, C. Pentangelo, F. Pellegatta, A. Crespi, and R. Osellame, "Low power reconfigurability and reduced crosstalk in integrated photonic circuits fabricated by femtosecond laser micromachining," Laser Photonics Rev. **14**, 2000024 (2020).

[16] *Femtosecond Laser Micromachining: Photonic and Microfluidic Devices in Transparent Materials*, *Topics in Applied Physics*, edited by R. Osellame, G. Cerullo, and R. Ramponi (Springer, Berlin Heidelberg, 2012).

[17] S. Gross and M. J. Withford, "Ultrafast-laser-inscribed 3D integrated photonics: Challenges and emerging applications," Nanophotonics **4**, 332–352 (2015).

[18] B. Sun, F. Morozko, P. S. Salter, S. Moser, Z. Pong, R. B. Patel, I. A. Walmsley, M. Wang, A. Hazan, N. Barré, A. Jesacher, J. Fells, C. He, A. Katiyi, Z.-N. Tian, A. Karabchevsky, and M. J. Booth, "On-chip beam rotators, adiabatic mode converters, and wave plates through low-loss waveguides with variable cross-sections," Light: Sci. Appl. **11**, 214 (2022).

[19] A. Arriola, S. Gross, N. Jovanovic, N. Charles, P. G. Tuthill, S. M. Olaizola, A. Fuerbach, and M. J. Withford, "Low bend loss waveguides enable compact, efficient 3D photonic chips," Opt. Express **21**, 2978–2986 (2013).

[20] G. Corrielli, S. Atzeni, S. Piacentini, I. Pitsios, A. Crespi, and R. Osellame, "Symmetric polarization-insensitive directional couplers fabricated by femtosecond laser writing," Opt. Express **26**, 15101–15109 (2018).

[21] F. Flamini, L. Magrini, A. S. Rab, N. Spagnolo, V. D'Ambrosio, P. Mataloni, F. Sciarrino, T. Zandrini, A. Crespi, R. Ramponi, and R. Osellame, "Thermally reconfigurable quantum photonic circuits at telecom wavelength by femtosecond laser micromachining," Light: Sci. Appl. **4**, e354 (2015).

[22] A. Yariv, "Universal relations for coupling of optical power between microresonators and dielectric waveguides," Electron. Lett. **36**, 321–322 (2000).

[23] Q. Yang, "Finesse of ring resonators," AIP Adv. **13**, 085225 (2023).

[24] C. V. Cushman, B. A. Sturgell, A. C. Martin, B. M. Lunt, N. J. Smith, and M. R. Linford, "Eagle XG® glass, optical constants from 230 to 1690 nm (0.73–5.39 eV) by spectroscopic ellipsometry," Surf. Sci. Spectra **23**, 55–60 (2016).

[25] A. Ross-Adams, T. T. Fernandez, M. Withford, and S. Gross, "Low bend loss, high index, composite morphology ultra-fast laser written waveguides for photonic integrated circuits," Light: Adv. Manuf. **5**, 52–61 (2024).